Deducing density and strength of nanocrystalline Ta and diamond under extreme conditions from X-ray diffraction

Y. Y. Zhang,[a] M. X. Tang,[a] Y. Cai,[a] J. C. E[a]* and S. N. Luo[a,b]*

[a]The Peac Institute of Multiscale Sciences, Chengdu, Sichuan 610031, People's Republic of China, and [b]Key Laboratory of Advanced Technologies of Materials, Ministry of Education, Southwest Jiaotong University, Chengdu, Sichuan 610031, People's Republic of China. *Correspondence e-mail: jce@pims.ac.cn, sluo@pims.ac.cn

In situ X-ray diffraction with advanced X-ray sources offers unique opportunities for investigating materials properties under extreme conditions such as shock-wave loading. Here, Singh's theory for deducing high-pressure density and strength from two-dimensional (2D) diffraction patterns is rigorously examined with large-scale molecular dynamics simulations of isothermal compression and shock-wave compression. Two representative solids are explored: nanocrystalline Ta and diamond. Analysis of simulated 2D X-ray diffraction patterns is compared against direct molecular dynamics simulation results. Singh's method is highly accurate for density measurement (within 1%) and reasonable for strength measurement (within 10%), and can be used for such measurements on nanocrystalline and polycrystalline solids under extreme conditions (*e.g.* in the megabar regime).

1. Introduction

Knowledge of equation of state and strength of materials under extreme conditions is critical to exploiting or optimizing their performance in engineering applications, and to understanding the structure and dynamics of planetary interiors, but measurements of such properties (in particular strength) are still challenging. Extreme conditions are normally achieved with diamond anvil cell (DAC) or shock-wave compression. In DAC loading, X-ray diffraction (XRD) is often used to deduce lattice compression and strength (Singh, 1993; Uchida *et al.*, 1996; He & Duffy, 2006; Liermann *et al.*, 2010; Xiong *et al.*, 2014; Singh & Liermann, 2015; Dorfman *et al.*, 2015). For shock-wave loading (Murphy *et al.*, 2010; Hawreliak *et al.*, 2012; MacDonald *et al.*, 2016; Foster *et al.*, 2017), the yield strength is measured with stress gauges (Rosenberg, 2000), pressure-shear loading (Yuan *et al.*, 2001) and reshock–release loading (Lipkin & Asay, 1977; Asay & Lipkin, 1978; Asay & Chhabildas, 1981; Huang & Asay, 2007). Advanced X-ray sources such as synchrotron radiation sources, X-ray free-electron lasers (XFELs) and laser-induced plasma emission sources offer opportunities for probing materials properties with XRD, and have been applied to single crystals (Rigg & Gupta, 2001; Turneaure & Gupta, 2009, 2011; Comley *et al.*, 2013; Fan *et al.*, 2016) and polycrystalline solids (Hawreliak *et al.*, 2012; Fan *et al.*, 2014; Singh, 2014; Lu *et al.*, 2016; Briggs *et al.*, 2017; Foster *et al.*, 2017; Wehrenberg *et al.*, 2017).

For polycrystalline solids, a theory was developed by Singh for DAC experiments (Singh, 1993) to obtain density and strength from 2D XRD patterns (Singh, 2004, 2009, 2014; Singh *et al.*, 2012). Variations of Singh's theory were applied to shock-wave loading (Hawreliak *et al.*, 2012; MacDonald *et al.*,
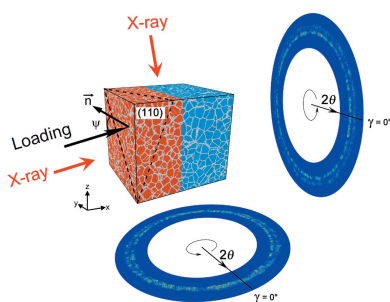
2016; Foster *et al.*, 2017). However, there are assumptions inherent in Singh's theory as regards deducing density and differential stress (yield strength), such as the small strain assumption (Singh, 1993; MacDonald *et al.*, 2016). Given the wide use of Singh's theory, it is highly desirable to examine rigorously its accuracy, and its applicability to extreme conditions. A self-consistent examination with minimum/zero assumptions is timely, considering that *in situ* temporally resolved XRD measurements with advanced X-ray sources have gained increasing importance in the study of materials under dynamic extremes (Wehrenberg *et al.*, 2017).

Here, we conduct large-scale molecular dynamics (MD) simulations combined with XRD simulations to compare the predictions of Singh's theory against direct MD simulations. We choose Ta and diamond as examples to represent 'soft' and 'hard' solids. Ta (Lu *et al.*, 2013; Wehrenberg *et al.*, 2017; Tang *et al.*, 2017; Sliwa *et al.*, 2018) and diamond (Knudson *et al.*, 2008; Bradley *et al.*, 2009; Smith *et al.*, 2014; MacDonald *et al.*, 2016; Gregor *et al.*, 2017) have been investigated both in experiments and simulations. MD simulations of nanocrystalline solids are not only interesting for their engineering applications but also allow us to evaluate the contribution of grain boundaries in compression in addition to that of crystal lattices, since diffraction peak positions only represent lattice compression. The challenges posed by diffuse scattering of nanocrystalline solids under shock compression (poor signal-to-noise ratio) can also be mitigated by highly coherent XFELs, and MD/XRD simulations are useful for such XFEL experiments in the future. Our results show that Singh's theory is highly accurate for density measurements (within 1%) and reasonably accurate for strength measurements (within 10%) under megabar conditions, and can be applied for both static and dynamic compression.

2. Methodology

2.1. Loading and diffraction geometries

For solids under extreme conditions, we consider two common types of loading, *i.e.* shock-wave and diamond anvil cell (DAC) compression; generally the bulk stress states are both axially symmetric. Shock-wave loading is adiabatic compression accompanied by heating, and DAC loading is normally an isothermal process (at 300 K as in our case, if no external heating or cooling is applied). We use the transmission geometry for diffraction calculations. Loading and diffraction geometries are both shown in Fig. 1.

The loading direction (the shock compression direction in Fig. 1) forms an angle of ψ with the normal (**n**) of a diffracting plane under consideration (here the {110} plane for Ta). ψ is referred to as the loading–diffraction geometry angle, and can be varied as desired. Two frequently used geometries, where the incident X-ray direction is parallel (the longitudinal geometry) or perpendicular (the transverse geometry) to the loading direction, are shown in Fig. 1.

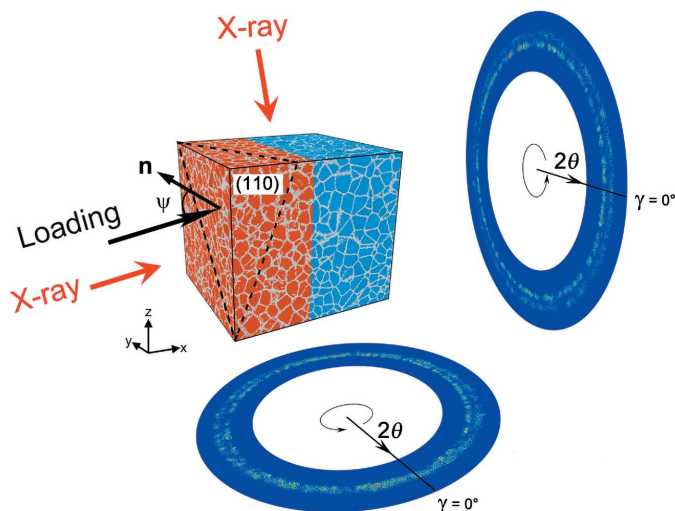In our discussion below, we consider only the transverse geometry, although the geometries can be arbitrary. For

Figure 1
Loading and diffraction geometries for dynamic X-ray diffraction measurements under extreme conditions. Here shock loading of nanocrystalline Ta is used as an example of loading. Longitudinal and transverse diffraction geometries are illustrated, referring to the cases with the incident X-ray direction being parallel or perpendicular to the loading direction, respectively. The dashed triangle refers to the {110} diffraction planes with a normal **n**. Loading-diffraction geometry angle ψ, diffraction angle 2θ and azimuthal angle γ are also defined.

diffraction, the 2D detector is set perpendicular to the incident X-ray direction (the normal detector position). For an arbitrary detector position, a geometrical correction can be applied so the detector position becomes normal. The diffraction angle (2θ) and azimuthal angle (γ) are defined on the detector, and there exists the following relation among ψ, 2θ and γ,

$$\cos \psi = \cos \theta \cos \gamma. \tag{1}$$

In the case shown in Fig. 1, two diffraction {110} rings appear from the unshocked and shocked regions, corresponding to the inner and outer rings, respectively. For isothermal DAC compression, the geometries are similar, and the loading direction is perpendicular to the culets of the diamond anvils.

2.2. Molecular dynamics simulations

For MD simulations of shock compression and isothermal DAC compression, the Large-scale Atomic/Molecular Massively Parallel Simulator (LAMMPS) (Plimpton, 1995) is used. The interatomic interactions in Ta are described with an embedded-atom method (EAM) potential (Ravelo *et al.*, 2013). This EAM potential is widely adopted for shock and nonshock simulations, especially for thermodynamic and mechanical properties (Wang *et al.*, 2014; Remington *et al.*, 2014), melting (Liu *et al.*, 2016) and equation of state (Ravelo *et al.*, 2012, 2013), which are in agreement with the experimental results (Marsh, 1980; Mitchell & Nellis, 1981; Cynn & Yoo, 1999) and *ab initio* calculations (Dewaele *et al.*, 2004). For diamond, we use the Tersoff potential (Tersoff, 1989), which has been used in the studies of carbon-based materials,

including diamonds (Tersoff, 1994; Shen & Chen, 2007; Remediakis *et al.*, 2008; Sha *et al.*, 2011; Zhao *et al.*, 2016; Huang *et al.*, 2018). Nanocrystalline Ta and diamond configurations with random grain crystallographic orientations and grain centers are constructed via the Voronoi tessellation method (Voronoï, 1908; E *et al.*, 2018*a*).

The nanocrystalline Ta configuration has dimensions of 100 nm × 80 nm × 80 nm and contains approximately 2500 grains (grain size ∼5 nm), corresponding to about 35 000 000 atoms. The nanocrystalline diamond configuration has dimensions of 120 nm × 30 nm × 30 nm, and contains 300 grains (grain size ∼10 nm) and approximately 19 000 000 atoms. The time step for integrating the equation of motion is 1 fs and the run times are up to 100 ps. Prior to DAC or shock compression, energy minimization of the configurations is performed with the conjugate gradient method, followed by relaxation with a constant-pressure-temperature ensemble at 300 K and zero pressure. 3D periodic boundary conditions are applied. Therefore, the structures are optimized with negligible internal stress.

To mimic DAC loading, a sample is compressed with the lateral confinement. The loading axis is along the x-axis and 3D periodic boundary conditions are applied, the constant-volume-temperature ensemble (the 300 K isotherm) is used, and the dimension along the loading axis is reduced at a fixed decrement. Shock loading is also applied along the x-axis via a rigid piston (Holian & Lomdahl, 1998), and periodic boundary conditions are applied only along the y- and z-axes. The microcanonical ensemble is used for shock loading. Piston velocity (u_{p}) is varied to achieve different shock states. The stress tensor (σ_{ij}) is calculated after the removal of the velocity of the center of mass (Luo *et al.*, 2009). Hydrostatic compression is also performed with the constant-pressure-temperature ensemble at the equivalent hydrostatic stress (σ_{P}) corresponding to a 1D strain state for shock or isothermal compression.

The stress tensor can be decomposed into hydrostatic and deviatoric stress components as

$$\begin{pmatrix} \sigma_{xx} & 0 & 0 \\ 0 & \sigma_{yy} & 0 \\ 0 & 0 & \sigma_{zz} \end{pmatrix} = \sigma_{\mathrm{P}}\,\mathbf{I} + \begin{bmatrix} (2/3)t & 0 & 0 \\ 0 & -(1/3)t & 0 \\ 0 & 0 & -(1/3)t \end{bmatrix},$$

where $\mathbf{I}$ is the identity matrix, $\sigma_{xx} \geq \sigma_{yy} = \sigma_{zz}$ for homogeneous isotropic solids, $\sigma_{\mathrm{P}} = (1/3)(\sigma_{xx} + \sigma_{yy} + \sigma_{zz})$ represents the mean normal stress or so-called equivalent hydrostatic stress, and $t = \sigma_{xx} - (1/2)(\sigma_{yy} + \sigma_{zz})$ denotes the differential stress. According to the von Mises yield criterion (Ruoff, 1975), $t = \sigma_{\mathrm{Y}} = 2\tau$ upon yield. σ_{Y} and τ are the (residual) yield strength and maximum shear stress, respectively. t and bulk density ρ are obtained directly from MD simulations, and compared with those from X-ray diffraction analysis as shown below.

2.3. Diffraction simulation and analysis

Given the atomic configurations at different loading states, we calculate corresponding diffraction patterns with *GAPD*, a GPU-accelerated parallel diffraction simulation code (E *et al.*, 2018*b*). The diffraction intensity I at scattering vector $\mathbf{q}$ is the product of atom number N, structure factor $F(\mathbf{q})$ and its complex conjugate, $F^*(\mathbf{q})$ (Warren, 1969; Chen *et al.*, 2017),

$$I(\mathbf{q}) = \frac{F^*(\mathbf{q})\,F(\mathbf{q})}{N}, \tag{2}$$

with

$$F(\mathbf{q}) = \sum_{j=1}^{N} f_j \exp\!\left(2\pi i \mathbf{q} \cdot \mathbf{r}_j\right). \tag{3}$$

Here, $\mathbf{r}_j$ is the position of the jth atom in real space, and f_j is the atomic scattering factor of atom j. Then, we obtain the diffraction patterns projected from reciprocal space to a two-dimensional detector. An example is shown in Fig. 2(*a*) with the corresponding distribution of ψ [defined in equation (1)] illustrated in Fig. 2(*b*). The X-ray wavelength in our calculations is 1 Å (12.398 keV), 2θ ranges from $20°$ to $35°$, and the corresponding range of ψ is $10°-90°$.
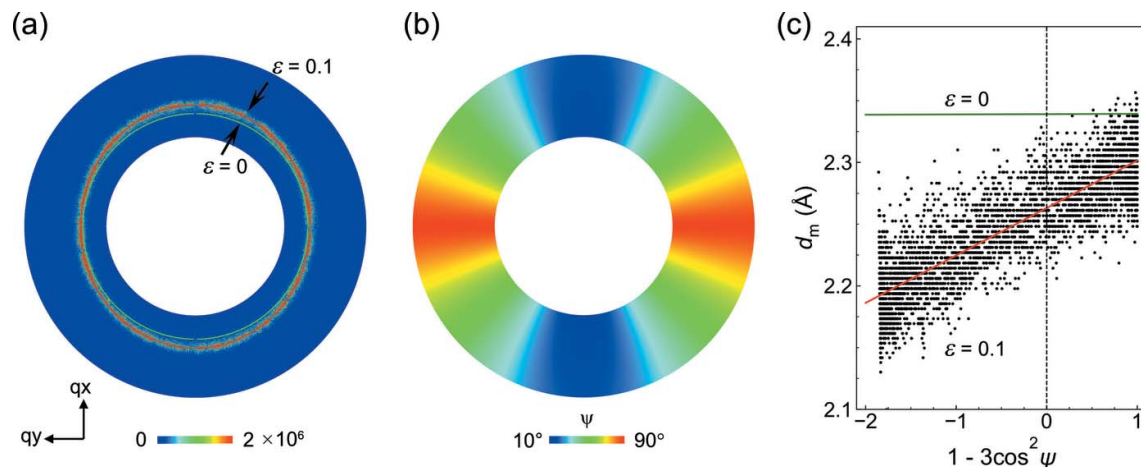
Figure 2
(*a*) 2D diffraction patterns (the {110} reflection) for nanocrystalline Ta at different strains (ε_{xx} or simply ε) under isothermal compression (DAC). (*b*) Distribution of ψ on the 2D diffraction patterns for the transverse geometry. (*c*) Corresponding d_{m} versus $(1 - 3\cos^2 \psi)$ plots. The solid curves in (*a*) and (*c*) denote fitting based on equation (4).

From 2D X-ray diffraction patterns, we can deduce bulk density under the equivalent hydrostatic pressure density (ρ_P) and strength under extreme conditions using a method originally presented by Singh (1993) in the small strain limit, and compare the results with those obtained from direct MD simulations. In this theory, a polycrystalline sample is compressed and the stress field is axially symmetric along the loading axis (the x-axis).

The measured lattice spacing, $d_m(hkl)$, is related to ψ via

$$d_m(hkl) = d_P(hkl)\left[1 + \left(1 - 3\cos^2\psi\right)Q(hkl)\right]. \qquad (4)$$

Here, $d_P(hkl)$ denotes d-spacing due to σ_P, and $Q(hkl)$ is a factor which depends on t and single-crystal elastic compliances, S_{ij}. Since $d_m = \lambda/2\sin\theta$, we obtain a scatter plot of d_m versus $(1 - 3\cos^2\psi)$, which can then be fitted with equation (4). The fitting in the d_m versus $(1 - 3\cos^2\psi)$ plane is mapped back into the detector plane to obtain the fitted diffraction rings. The 2D diffraction patterns and d_m versus $(1 - 3\cos^2\psi)$ plots along with their fittings are shown in Figs. 2(a) and 2(c), respectively. The shape of a diffraction ring is a perfect circle if strain free, and it becomes elliptical (or other noncircular shapes) under a finite strain. In the d_m versus $(1 - 3\cos^2\psi)$ plots, the intercept at $(1 - 3\cos^2\psi) = 0$ is d_P, and the slope is $d_P(hkl)\,Q(hkl)$. The slope is zero for the strain-free cases.

For convenience, we define relative density $\rho^r = \rho/\rho_0$, where ρ_0 is the initial density. We use ρ_P^r to denote relative density under equivalent hydrostatic stress. ρ^r and ρ_P^r can be different, since their exact stress conditions are different. In equation-of-state measurements under nonhydrostatic compression, ρ_P^r rather than ρ^r should be used in principle.

Given d_P obtained from the diffraction analysis, we have

$$\rho_P^r(\varepsilon_{xx}) = \left[\frac{d_P(\varepsilon_{xx} = 0)}{d_P(\varepsilon_{xx})}\right]^3 \qquad (5)$$

for 1D strain conditions simulated in this work; the ρ_P^r values from XRD can be compared with those directly from MD simulations. Strictly speaking, $\rho_{P,XRD}^r$ only represents the bulk density of crystal lattices, while its MD counterpart, $\rho_{P,MD}^r$, consists of contributions from both lattices and grain boundaries. Therefore, XRD measurements may underestimate density by a small amount, since grain boundaries in a polycrystalline sample overall are more compressible than crystal lattices.

The residual strength t is then given by

$$t = 6G \langle Q(hkl)\rangle f(x, \alpha), \qquad (6)$$

where G is the aggregate shear modulus, x is the elastic anisotropy factor and α is a weight factor depending on x. $f(x, \alpha)$ is a parameter, approximately 1 for all crystal systems (Singh, 2014). In theory, the aggregate shear modulus G is expressed as the harmonic mean of G_V and G_R,

$$\frac{1}{G} = \frac{1}{2}\left(\frac{1}{G_V} + \frac{1}{G_R}\right). \qquad (7)$$

Here, G_V is the aggregate shear modulus under the Voigt assumption (strain continuity) (Voigt, 1928), and G_R is the

aggregate shear modulus under the Reuss assumption (stress continuity) (Reuss, 1929). For better accuracy, the aggregate shear modulus G under extreme conditions is calculated directly from MD simulations. In MD simulations, small shear strains are applied to the sample followed by stress tensor calculation. Then the shear modulus is calculated from stress and strain tensors.

3. Results and discussion

3.1. Nanocrystalline Ta

For nanocrystalline Ta, we apply both isothermal compression (or DAC) and shock compression. For isothermal compression at 300 K (strain rate $\sim 10^9\,\mathrm{s}^{-1}$), ε_{xx} (or simply ε) varies from 0 to 0.4, and, for shock compression (strain rate $\sim 10^{11}\,\mathrm{s}^{-1}$), the piston velocity u_P varies from 0 to 1.5 km s^{-1}. The initial configurations are the same for isothermal DAC compression and shock compression. MD simulation results and XRD analysis are presented in Figs. 2–5 and Tables 1–4.

For isothermal compression, the stress–strain curves directly obtained from MD simulations are shown in Fig. 3, including $\sigma_{xx}(\varepsilon_{xx})$, $\sigma_P(\varepsilon_{xx})$ and $t(\varepsilon_{xx})$. σ_{xx} and σ_P increase monotonically to >270 GPa with ε_{xx} increasing to 0.4, while the differential stress increases rapidly to the peak (6 GPa at $\varepsilon_{xx} = 0.08$; the elastic regime), followed by relaxation (yield) and strain hardening beginning at $\varepsilon_{xx} \simeq 0.2$. Full stress and relative density parameters are shown in Table 1 at representative strains, $\varepsilon_{xx} = 0$, 0.1, 0.2, 0.3 and 0.4.

For 2D diffraction pattern analysis of isothermal compression, we consider the following cases: $\varepsilon_{xx} = 0$, 0.1, 0.2, 0.3 and 0.4. The diffraction patterns of the strongest reflection, the {110} reflection, are shown in Fig. 4, along with the fitted diffraction rings. The diffraction patterns show strong diffuse scattering features due to the small grain size. Compared with the diffraction ring at zero strain, the diffraction ring moves toward larger 2θ with increasing strain, and its shape deviates from the circular shape as a result of nonhydrostatic compression. The 2D diffraction patterns are reduced to the $d_m(110)$ versus $(1 - 3\cos^2\psi)$ plots, which are fitted with the
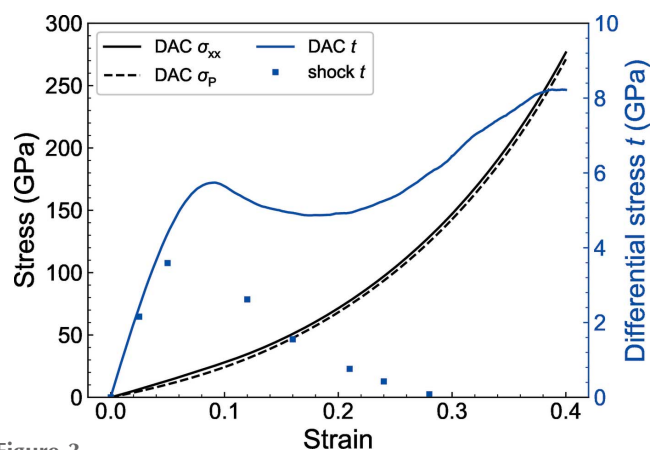

Figure 3
Nanocrystalline Ta: the stress versus strain (ε_{xx}) curves for isothermal compression (DAC), along with differential stresses for shock compression (squares).

Table 1
Isothermal (DAC) compression of nanocrystalline Ta: direct MD simulations.

ρ_P^r refers to compression under equivalent hydrostatic stress.

ε_{xx}	σ_{xx} (GPa)	σ_P (GPa)	t (GPa)	ρ^r	ρ_P^r
0.0	0.00	0.00	0.00	1.000	1.000
0.1	28.01	24.25	5.65	1.111	1.111
0.2	71.45	68.20	4.92	1.250	1.251
0.3	147.08	142.83	6.45	1.429	1.429
0.4	276.69	271.20	8.23	1.667	1.666

Table 2
Isothermal (DAC) compression of nanocrystalline Ta: XRD analysis.

Relative errors are $\epsilon_t \equiv t/t_{MD} - 1$; $\epsilon_{\rho 1} \equiv \rho^r/\rho_{MD}^r - 1$; $\epsilon_{\rho 2} \equiv \rho_P^r/\rho_{PMD}^r - 1$.

ε_{xx}	d_P (Å)	Q	t (GPa)	ϵ_t (%)	ρ_P^r	$\epsilon_{\rho 1}$ (%)	$\epsilon_{\rho 2}$ (%)
0.0	2.339	0.0001	0.03	–	1.000	–	–
0.1	2.263	0.0170	6.10	7.95	1.104	−0.63	−0.63
0.2	2.177	0.0119	4.77	−3.07	1.241	−0.72	−0.80
0.3	2.082	0.0108	6.44	−0.09	1.419	−0.70	−0.70
0.4	1.980	0.0115	8.77	6.56	1.650	−1.02	−0.96

linear equation [equation (5)]. For $\varepsilon_{xx} = 0$, $Q = 0$ as expected, and the slopes deviate from zero at higher strains: Q increases and then decreases with increasing strain.

Given the $d_m(110)$ versus $(1 - 3\cos^2\psi)$ fitting results at different ε_{xx}, we obtain d_P and Q as a function of the applied 1D strain ε_{xx}, and thus density and strength (differential stress) under elevated stresses (Table 2) and compare them with direct MD simulations (Table 1).

For nanocrystalline Ta under isothermal compression, the density under 1D strain compression (ρ^r; true density) agrees within 0.1% with that under equivalent hydrostatic compression (ρ_P^r) from direct MD simulations (Table 1). These two densities (ρ^r and ρ_P^r obtained directly from MD simulations) are used for calculating the relative errors in density obtained from the XRD analysis, denoted as $\epsilon_{\rho 1}$ and $\epsilon_{\rho 2}$ (Table 2), respectively. Similarly, the relative error in differential stress t obtained from the XRD analysis (ϵ_t; Table 2) is referenced to that directly obtained from MD simulations (Table 1).

The XRD analysis method is highly accurate for obtaining density and $|\epsilon_\rho| < 1\%$ for nanocrystalline Ta under isothermal compression (Table 2). Note that all $\epsilon_\rho < 0$; the negative values

of ϵ_ρ are due to the fact that the diffraction positions represent lattice deformation only, while the density values obtained directly from MD simulations have contributions from grain boundaries and crystal lattices, and are higher since grain boundaries are overall more compressible than crystal lattices. The accuracy in differential stress is reasonable, $|\epsilon_t| < 8\%$. While the measurement on Q is of high accuracy, converting Q to t involves different assumptions as discussed in Section 2, which may lead to systematic errors in deducing t.

Shock loading induces pure elastic compression for $u_p \leq 0.2$ km s^{-1} and elastic–plastic compression for $0.2 < u_p \leq 1.5$ km s^{-1}. The shock parameters from MD simulations are presented in Table 3 and Fig. 3. During elastic compression, the differential stress from shock loading is nearly identical to that in isothermal DAC compression, while it decreases rapidly for stronger shocks (after yield), and a complete loss of strength occurs at $u_p = 1.5$ km s^{-1}. The difference between DAC and shock loading in differential stress at higher strains is due to increased shock heating with increasing piston velocities/strains (the shock temperature is about 2800 K at $u_p = 1.5$ km s^{-1}).

For nanocrystalline Ta under shock compression, the 2D diffraction patterns are obtained along with fitted diffraction rings for piston velocity ranging from 0 to 1.5 km s^{-1}. The diffraction signals (Fig. 5) become more diffuse compared with isothermal loading (300 K) at similar strains (Fig. 4), due to shock-induced heating (the shock temperature is about 1300 K at $u_p = 1.0$ km s^{-1}). The 2D XRD patterns are reduced to the $d_m - (1 - 3\cos^2\psi)$ curves fitted with equation (5). The results are summarized in Table 3 for direct MD simulations and in Table 4 for XRD analysis.

Similar to isothermal compression, the densities under the actual shock-loading conditions (ρ^r) and the equivalent hydrostatic stress (ρ_P^r) are nearly identical (Table 3). The XRD analysis method is also highly accurate for shock compression (Tables 3 and 4). The densities obtained from XRD agree with direct MD simulations to within 1%, and all $\epsilon_\rho < 0$ as expected. The relative errors in differential stress are within 4%.

3.2. Nanocrystalline diamond

In sharp contrast to metals, diamond has the highest yield strength and low compressibility, and represents the other end
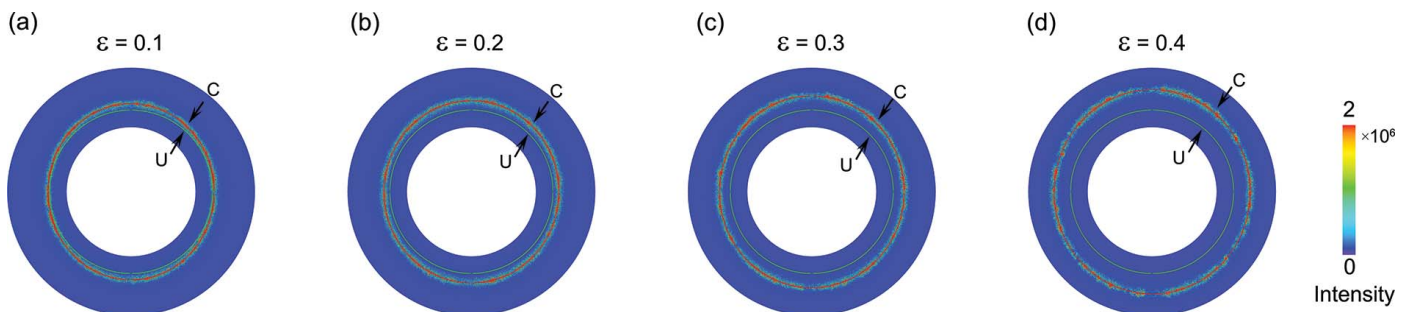
Figure 4
2D diffraction patterns (the {110} reflection) of nanocrystalline Ta under isothermal compression (DAC) at different strains (ε_{xx}). The solid curves denote fitting with equation (4). The inner different rings refer to zero strain. 2θ ranges from 20° to 35°. U: uncompressed; C: compressed.

Table 3
Shock loading of nanocrystalline Ta: direct MD simulations.

u_p (km s^{-1})	σ_{xx} (GPa)	σ_P (GPa)	t (GPa)	ε_{xx}	ρ^r	ρ_P^r
0.0	0.00	0.00	0.00	0.00	1.000	1.000
0.2	12.91	10.51	3.59	0.05	1.053	1.053
0.5	33.62	31.88	2.62	0.12	1.137	1.138
1.0	77.56	77.05	0.76	0.21	1.267	1.268

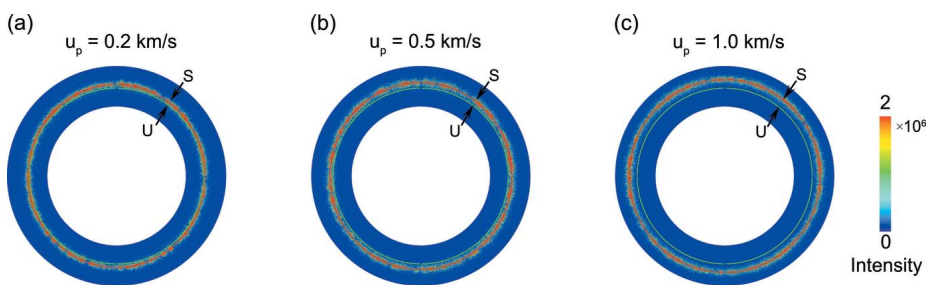**Table 4**
Shock loading of nanocrystalline Ta: XRD analysis.

Here $\epsilon_t \equiv t/t_{MD} - 1$; $\epsilon_{\rho1} \equiv \rho^r/\rho_{MD}^r - 1$; $\epsilon_{\rho2} \equiv \rho_P^r/\rho_{P,MD}^r - 1$.

u_p (km s^{-1})	d_P (Å)	Q	t (GPa)	ϵ_t (%)	ρ_P^r	$\epsilon_{\rho1}$ (%)	$\epsilon_{\rho2}$ (%)
0.0	2.339	0.0001	0.03	–	1.000	–	–
0.2	2.301	0.0103	3.64	1.34	1.050	−0.28	−0.28
0.5	2.247	0.0073	2.54	−3.13	1.128	−0.79	−0.88
1.0	2.166	0.0020	0.75	−1.59	1.260	−0.55	−0.63

Table 5
Shock loading of nanocrystalline diamond: direct MD simulations.

u_p (km s^{-1})	σ_{xx} (GPa)	σ_P (GPa)	t (GPa)	ε_{xx}	ρ^r	ρ_P^r
0.0	0.02	−0.04	0.08	0.00	1.000	1.000
3.0	192.40	103.22	133.77	0.16	1.188	1.199

Table 6
Shock loading of nanocrystalline diamond: XRD analysis.

Here $\epsilon_t \equiv t/t_{MD} - 1$; $\epsilon_{\rho1} \equiv \rho^r/\rho_{MD}^r - 1$; $\epsilon_{\rho2} \equiv \rho_P^r/\rho_{P,MD}^r - 1$.

u_p (km s^{-1})	d_P (Å)	Q	t (GPa)	ϵ_t (%)	ρ_P^r	$\epsilon_{\rho1}$ (%)	$\epsilon_{\rho2}$ (%)
0.0	2.069	0.0012	3.29	–	1.000	–	–
3.0	1.960	0.0393	134.35	0.43	1.177	−0.93	−1.83

of the wide spectrum of materials. Deducing the equation of state and strength of polycrystalline diamonds at extreme conditions is of direct technical and scientific interest (Field, 1992; Eremets *et al.*, 2005; Bradley *et al.*, 2009; Lang & Gupta, 2010; McWilliams *et al.*, 2010). As another validation and application case, we investigate below shock compression of nanocrystalline diamond and XRD interpretation as regards density and strength at high pressures.

Shock loading with a piston velocity u_p = 3.0 km s^{-1} is used for illustrative purposes here. At this piston velocity, nano-crystalline diamond undergoes the elastic–plastic transition. The corresponding 2D diffraction pattern of nanocrystalline diamond at the steady shock state is obtained [Fig. 6(*a*)]; the pattern is relatively spotty compared with the nanocrystalline Ta cases, since we deliberately decrease the grain number and increase grain size to check their effects on data analysis. For comparison, the XRD pattern is also calculated for the unshocked sample. Fittings to both 2D diffraction patterns are performed based on equation (5) and plotted as a solid curve in Fig. 6(*a*), and the corresponding d_m versus $(1 - 3\cos^2\psi)$ plots and linear fittings are shown in Fig. 6(*b*). The MD results and XRD analysis are also summarized in Tables 5 and 6.

Figure 6
Nanocrystalline diamond under shock compression. (*a*) 2D {110} diffraction patterns from the unshocked (U) and shocked (S) samples, and (*b*) the corresponding d_m versus $(1 - 3\cos^2\psi)$ plots. The solid curves are fittings based on equation (4).

The shocked sample displays a highly elliptical diffraction ring and a large slope ($Q = 0.0393$), and the unshocked sample displays a perfectly circular diffraction ring and zero slope ($Q = 0$) as expected. The density from the 2D diffraction pattern analysis at u_p = 3.0 km s^{-1} is still of high accuracy, with an underestimate by 0.93% relative to the true density and by 1.8% with respect to the density under equivalent hydrostatic stress. This underestimate is again due to different compressibilities of grain boundaries and crystal lattices. However, ρ^r and ρ_P^r differ more in the diamond case (Table 5) than the Ta case, likely due to the more pronounced nonhydrostaticity in nanocrystalline diamond.

The shear modulus of diamond under this high pressure is calculated as 570.19 GPa from MD simulations, so the differential stress from XRD analysis is t_{XRD} = 134.35 GPa [equation (7)] under the equivalent hydrostatic pressure of 103.22 GPa, almost identical to that from direct MD simulations (t_{MD} = 133.77 GPa, differing only by 0.4%).

Figure 5
2D diffraction patterns of nanocrystalline Ta (the {110} reflection) under shock compression at different piston velocities (u_p). The solid curves denote fittings. The diffraction ring for the unshocked state is also included for comparison. 2θ ranges from 20° to 30°. U: unshocked; S: shocked.
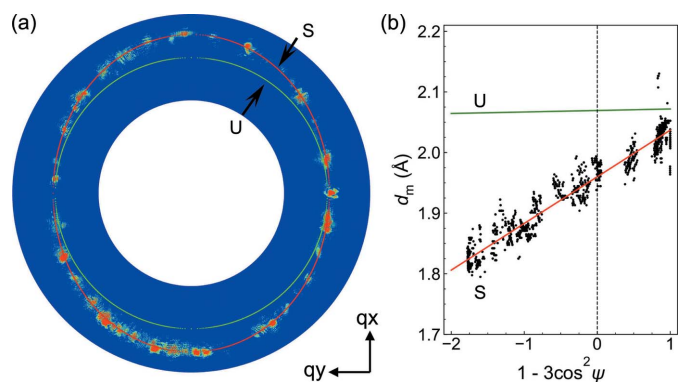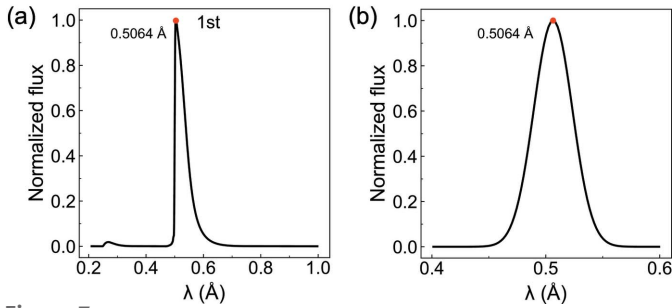
Figure 7
(a) Simulated X-ray spectrum from a typical APS undulator source (U18Gap13), through a 1 mm × 1 mm pinhole located 35 m away from the source. U18Gap13: undulator with a period of 18 mm and a gap of 13 mm; electron energy is 7 GeV and the current is 100 mA. The spectral flux is normalized by the peak value. (b) Gaussian-shaped spectrum (8% bandwidth). Both spectra peak at 0.5604 Å.
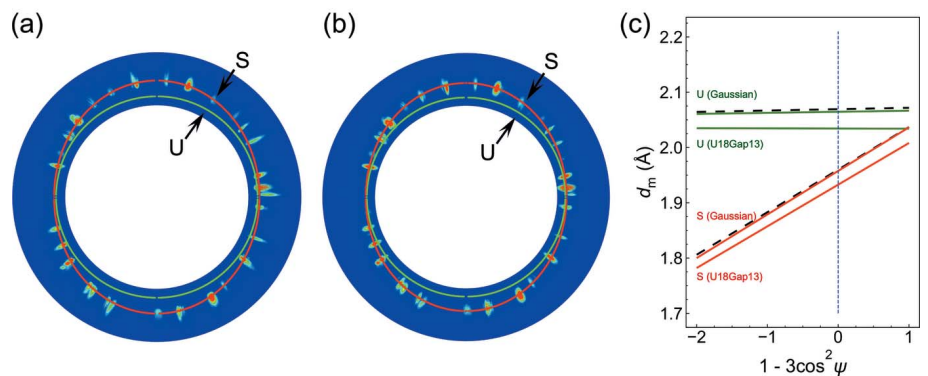
3.3. Implications to synchrotron experiments

Two key issues for synchrotron experiments are q-resolution and the effects of X-ray spectral characteristics (bandwidth and spectrum shape). We discuss briefly below these two issues considering realistic detector sizes, detector geometry and X-ray spectra.

In experiment, pixel size and sample-to-detector distance (L_{sd}) affect the q-resolution. For instance, we consider the Ta case with a piston velocity of 1 km s^{-1}, and take L_{sd} = 100 mm for calculating the {110} diffraction ring. For a typical pixel size (100 µm × 100 µm), a single pixel represents a 0.045° difference in 2θ in this geometry, corresponding to 0.5% density variation. The full {110} diffraction ring can be recorded on a 115 mm × 115 mm detector (1150 pixels × 1150 pixels). The length difference between the major and minor axes of the diffraction ring (ellipse) is 2.24 mm, and the difference in 2θ is 1°; such an ellipticity of the diffraction ring can be readily resolved. Similarly, it can be resolved for a 200 µm × 200 µm pixel size.

In addition to monochromatic X-rays, we also explore spectra with finite bandwidths and different spectrum symmetries. Here, we choose the first harmonic of an undulator source (U18Gap13) at the Advanced Photon Source (APS) beamline 32ID-B [Fig. 7(a)]. This asymmetrical pink beam has a bandwidth of 8% with its spectral flux peak located at λ_c = 0.5064 Å. Another symmetric Gaussian-shaped spectrum with the same spectral peak wavelength and bandwidth is examined for comparison [Fig. 7(b)]. The bandwidths are considerably larger than those of XFELs.

The simulated 2D {110} peak beam diffraction patterns are shown in Figs. 8(a) and 8(b). To reduce the pink beam diffraction patterns with Singh's method, we use the peak wavelength λ_c, and obtain the corresponding d_m versus $(1 - 3\cos^2\psi)$ curves in Fig. 8(c). The

Table 7
Shock loading of nanocrystalline diamond: pink beam X-ray diffraction with the first harmonic of the U18Gap13 undulator spectrum.

Here $\epsilon_t \equiv t/t_{MD} - 1$; $\epsilon_{\rho1} \equiv \rho^r/\rho^r_{MD} - 1$; $\epsilon_{\rho2} \equiv \rho^r_P/\rho^r_{P,MD} - 1$.

u_P (km s^{-1})	d_P (Å)	Q	t (GPa)	ϵ_t (%)	ρ^r_P	$\epsilon_{\rho1}$ (%)	$\epsilon_{\rho2}$ (%)
0.0	2.034	−0.0003	−3.29	–	1.000	–	–
3.0	1.933	0.0390	133.42	−0.26	1.166	−1.85	−2.75

Table 8
Shock loading of nanocrystalline diamond: pink beam X-ray diffraction with the Gaussian-shaped spectrum.

Here $\epsilon_t \equiv t/t_{MD} - 1$; $\epsilon_{\rho1} \equiv \rho^r/\rho^r_{MD} - 1$; $\epsilon_{\rho2} \equiv \rho^r_P/\rho^r_{P,MD} - 1$.

u_P (km s^{-1})	d_P (Å)	Q	t (GPa)	ϵ_t (%)	ρ^r_P	$\epsilon_{\rho1}$ (%)	$\epsilon_{\rho2}$ (%)
0.0	2.065	0.0009	3.20	–	1.000	–	–
3.0	1.958	0.0403	137.74	2.96	1.173	−1.26	−2.17

analysis results for the pink beam sources are presented in Tables 7 and 8. Compared with the monochromatic X-ray diffraction, the intercept is slightly smaller and the slope remains the same for the U18Gap13 spectrum, while the fitting curves for the Gaussian-shaped spectrum coincide with those for the monochromatic diffraction. The change of intercept in Fig. 8(c) for the U18Gap13 spectrum represents the diffraction peak shift due to the asymmetry of the pink beam spectrum (E et al., 2018b). Therefore, the strength, which is calculated with the slope, is not affected by the spectrum width or symmetry, while there is a slight overestimate of density due to asymmetry of the undulator source U18Gap13. The overall accuracy in relative density is within 3%.

4. Conclusions

The accuracy of determining density and strength from a 2D diffraction pattern (Singh's theory) is examined independently with direct large-scale MD simulations and simulated 2D diffraction patterns, under representative extreme compres-

Figure 8
Pink beam X-ray diffraction of nanocrystalline diamond. 2D {110} diffraction patterns from the unshocked (U) and shocked (S) samples with (a) the first harmonic of U18Gap13 and (b) a Gaussian-shaped spectrum. (c) Corresponding d_m versus $(1 - 3\cos^2\psi)$ plots. The dashed curves refer to monochromatic XRD, and solid curves to the pink beam.

sion conditions (DAC and shock compression) of two representative solids, nanocrystalline Ta and diamond. Our results highlight the necessity of 2D diffraction pattern analysis for the equation of state, and the usefulness for strength measurements.

(i) Singh's theory is validated self-consistently for isothermal compression as in DAC experiments, and its extension to shock compression appears to be reliable.

(ii) Singh's theory is highly accurate for determining true density (within 1%), but always underestimates density since it only considers lattice compression, since grain boundaries are overall more compressible than crystal lattices.

(iii) The residual strength can achieve an accuracy of <8% or better, although improvement is desirable.

(iv) Small-strain assumption appears to be valid to large strains, for small (nanocrystalline) as well as large grain sizes. A full diffraction ring rather than the magic angle ($\psi = 54.7°$) should be measured whenever possible for better accuracy.

(v) For nanocrystalline Ta, isothermal compression leads to a decrease of strength followed by increased strength after yield, while shock compression results in decrease or loss of strength for strong shocks (below 100 GPa) due to shock heating. Nanocrystalline diamond retains its exceptional strength even above 100 GPa.

(vi) For pink beam X-ray diffraction, the slope of a d_m versus $(1 - 3\cos^2 \psi)$ curve remains unchanged regardless of spectrum width or symmetry; however, the intercept (thus, density) may be over- or underestimated for asymmetric spectra.

References

Asay, J. R. & Chhabildas, L. C. (1981). In *Shock Waves and High-Strain-Rate Phenomena in Metals*, pp. 417–431. Springer.
Asay, J. R. & Lipkin, J. (1978). *J. Appl. Phys.* **49**, 4242–4247.
Bradley, D. K., Eggert, J. H., Smith, R. F., Prisbrey, S. T., Hicks, D. G., Braun, D. G., Biener, J., Hamza, A. V., Rudd, R. E. & Collins, G. W. (2009). *Phys. Rev. Lett.* **102**, 075503.
Briggs, R., Gorman, M. G., Coleman, A. L., McWilliams, R. S., McBride, E. E., McGonegle, D., Wark, J. S., Peacock, L., Rothman, S., Macleod, S. G., Bolme, C. A., Gleason, A. E., Collins, G. W., Eggert, J. H., Fratanduono, D. E., Smith, R. F., Galtier, E., Granados, E., Lee, H. J., Nagler, B., Nam, I., Xing, Z. & McMahon, M. I. (2017). *Phys. Rev. Lett.* **118**, 025501.
E, J. C., Cai, Y., Zhong, Z. Y., Tang, M. X., Zhu, X. R., Wang, L. & Luo, S. N. (2018a). *J. Appl. Cryst.* **51**, 124–132.
Chen, S., E, J. & Luo, S.-N. (2017). *J. Appl. Cryst.* **50**, 951–958.
Comley, A. J., Maddox, B. R., Rudd, R. E., Prisbrey, S. T., Hawreliak, J. A., Orlikowski, D. A., Peterson, S. C., Satcher, J. H., Elsholz, A. J.,
Park, H.-S., Remington, B. A., Bazin, N., Foster, J. M., Graham, P., Park, N., Rosen, P. A., Rothman, S. R., Higginbotham, A., Suggit, M. & Wark, J. S. (2013). *Phys. Rev. Lett.* **110**, 115501.
Cynn, H. & Yoo, C.-S. (1999). *Phys. Rev. B*, **59**, 8526–8529.
Dewaele, A., Loubeyre, P. & Mezouar, M. (2004). *Phys. Rev. B*, **70**, 094112.
Dorfman, S. M., Shieh, S. R. & Duffy, T. S. (2015). *J. Appl. Phys.* **117**, 065901.
E, J. C., Wang, L., Chen, S., Zhang, Y. Y. & Luo, S. N. (2018). *J. Synchrotron Rad.* **25**, 604–611.
Eremets, M. I., Trojan, I. A., Gwaze, P., Huth, J., Boehler, R. & Blank, V. D. (2005). *Appl. Phys. Lett.* **87**, 141902.
Fan, D., Huang, J. W., Zeng, X. L., Li, Y. E. J., Huang, J. Y., Sun, T., Fezzaa, K., Wang, Z. & Luo, S. N. (2016). *Rev. Sci. Instrum.* **87**, 053903.
Fan, D., Lu, L., Li, B., Qi, M. L. E. J., Zhao, F., Sun, T., Fezzaa, K., Chen, W. & Luo, S. N. (2014). *Rev. Sci. Instrum.* **85**, 113902.
Field, J. E. (1992). Editor. *The Properties of Natural and Synthetic Diamond.* London: Academic Press.
Foster, J. M., Comley, A. J., Case, G. S., Avraam, P., Rothman, S. D., Higginbotham, A., Floyd, E. K. R., Gumbrell, E. T., Luis, J. J. D., McGonegle, D., Park, N. T., Peacock, L. J., Poulter, C. P., Suggit, M. J. & Wark, J. S. (2017). *J. Appl. Phys.* **122**, 025117.
Gregor, M. C., Fratanduono, D. E., McCoy, C. A., Polsin, D. N., Sorce, A., Rygg, J. R., Collins, G. W., Braun, T., Celliers, P. M., Eggert, J. H., Meyerhofer, D. D. & Boehly, T. R. (2017). *Phys. Rev. B*, **95**, 144114.
Hawreliak, J., El-dasher, B., Eggert, J., Rygg, J., Collins, G. W., Lorenzana, H., Kimminau, G., Higginbotham, A., Nagler, B., Vinko, S., Murphy, W., Whitcher, T., Rothman, S., Park, N. & Wark, J. (2012). *AIP Conf. Proc.* **1426**, 975–978.
He, D. & Duffy, T. S. (2006). *Phys. Rev. B*, **73**, 134106.
Holian, B. L. & Lomdahl, P. S. (1998). *Science*, **280**, 2085–2088.
Huang, C., Peng, X., Yang, B., Chen, X., Li, Q., Yin, D. & Fu, T. (2018). *Carbon*, **136**, 320–328.
Huang, H. & Asay, J. R. (2007). *J. Appl. Phys.* **101**, 063550.
Knudson, M. D., Desjarlais, M. P. & Dolan, D. H. (2008). *Science*, **322**, 1822–1825.
Lang, J. M. & Gupta, Y. M. (2010). *J. Appl. Phys.* **107**, 113538.
Liermann, H.-P., Jain, A., Singh, A. K. & Saxena, S. K. (2010). *J. Phys. Chem. Solids*, **71**, 1088–1093.
Lipkin, J. & Asay, J. R. (1977). *J. Appl. Phys.* **48**, 182–189.
Liu, C. M., Xu, C., Cheng, Y., Chen, X. R. & Cai, L. C. (2016). *Appl. Phys. A*, **122**, 22.
Lu, C. H., Remington, B. A., Maddox, B. R., Kad, B., Park, H. S., Kawasaki, M., Langdon, T. G. & Meyers, M. A. (2013). *Acta Mater.* **61**, 7767–7780.
Lu, L., Huang, J. W., Fan, D., Bie, B. X., Sun, T., Fezzaa, K., Gong, X. L. & Luo, S. N. (2016). *Acta Mater.* **120**, 86–94.
Luo, S.-N., Germann, T. C. & Tonks, D. L. (2009). *J. Appl. Phys.* **106**, 123518.
MacDonald, M. J., Vorberger, J., Gamboa, E. J., Drake, R. P., Glenzer, S. H. & Fletcher, L. B. (2016). *J. Appl. Phys.* **119**, 215902.
McWilliams, R. S., Eggert, J. H., Hicks, D. G., Bradley, D. K., Celliers, P. M., Spaulding, D. K., Boehly, T. R., Collins, G. W. & Jeanloz, R. (2010). *Phys. Rev. B*, **81**, 014111.
Marsh, S. P. (1980). *LASL Shock Hugoniot Data*, Vol. 5. University of California Press.
Mitchell, A. C. & Nellis, W. J. (1981). *J. Appl. Phys.* **52**, 3363–3374.
Murphy, W. J., Higginbotham, A., Kimminau, G., Barbrel, B., Bringa, E. M., Hawreliak, J., Kodama, R., Koenig, M., McBarron, W., Meyers, M. A., Nagler, B., Ozaki, N., Park, N., Remington, B., Rothman, S., Vinko, S. M., Whitcher, T. & Wark, J. S. (2010). *J. Phys. Condens. Matter*, **22**, 065404.
Plimpton, S. (1995). *J. Comput. Phys.* **117**, 1–19.
Ravelo, R., An, Q., Germann, T. C. & Holian, B. L. (2012). *AIP Conf. Proc.* **1426**, 1263–1266.
Ravelo, R., Germann, T. C., Guerrero, O., An, Q. & Holian, B. L. (2013). *Phys. Rev. B*, **88**, 134101.

Remediakis, I. N., Kopidakis, G. & Kelires, P. C. (2008). *Acta Mater.* **56**, 5340–5344.

Remington, T. P., Ruestes, C. J., Bringa, E. M., Remington, B. A., Lu, C. H., Kad, B. & Meyers, M. A. (2014). *Acta Mater.* **78**, 378–393.

Reuss, A. (1929). *Z. Angew. Math. Mech.* **9**, 49–58.

Rigg, P. A. & Gupta, Y. M. (2001). *Phys. Rev. B*, **63**, 094112.

Rosenberg, Z. (2000). *AIP Conf. Proc.* **505**, 1033–1038.

Ruoff, A. L. (1975). *J. Appl. Phys.* **46**, 1389–1392.

Sha, Z. D., Branicio, P. S., Sorkin, V., Pei, Q. X. & Zhang, Y. W. (2011). *Diamond Relat. Mater.* **20**, 1303–1309.

Shen, L. & Chen, Z. (2007). *Int. J. Solids Struct.* **44**, 3379–3392.

Singh, A. K. (1993). *J. Appl. Phys.* **73**, 4278–4286.

Singh, A. K. (2004). *J. Phys. Chem. Solids*, **65**, 1589–1596.

Singh, A. K. (2009). *J. Appl. Phys.* **106**, 043514.

Singh, A. K. (2014). *J. Phys. Conf. Ser.* **500**, 122005.

Singh, A. K., Hu, J., Shu, J., Mao, H. & Hemley, R. J. (2012). *J. Phys. Conf. Ser.* **377**, 012008.

Singh, A. K. & Liermann, H.-P. (2015). *J. Appl. Phys.* **118**, 065903.

Sliwa, M., McGonegle, D., Wehrenberg, C., Bolme, C. A., Heighway, P. G., Higginbotham, A., Lazicki, A., Lee, H. J., Nagler, B., Park, H. S., Rudd, R. E., Suggit, M. J., Swift, D., Tavella, F., Zepeda-Ruiz, L., Remington, B. A. & Wark, J. S. (2018). *Phys. Rev. Lett.* **120**, 265502.

Smith, R. F., Eggert, J. H., Jeanloz, R., Duffy, T. S., Braun, D. G., Patterson, J. R., Rudd, R. E., Biener, J., Lazicki, A. E., Hamza, A. V., Wang, J., Braun, T., Benedict, L. X., Celliers, P. M. & Collins, G. W. (2014). *Nature*, **511**, 330–333.

Tang, M. X. E. J., Wang, L. & Luo, S. N. (2017). *J. Appl. Phys.* **121**, 115901.

Tersoff, J. (1989). *Phys. Rev. B*, **39**, 5566–5568.

Tersoff, J. (1994). *Phys. Rev. B*, **49**, 16349–16352.

Turneaure, S. J. & Gupta, Y. M. (2009). *J. Appl. Phys.* **106**, 033513.

Turneaure, S. J. & Gupta, Y. M. (2011). *J. Appl. Phys.* **109**, 123510.

Uchida, T., Funamori, N. & Yagi, T. (1996). *J. Appl. Phys.* **80**, 739–746.

Voigt, W. (1928). *Lehrbuch der Kristallphysik (mit Ausschluss der Kristalloptik).* Springer-Verlag.

Voronoï, G. (1908). *J. Reine Angew. Math.* **134**, 198–287.

Wang, L., Zhao, F., Zhao, F. P., Cai, Y., An, Q. & Luo, S. N. (2014). *J. Appl. Phys.* **115**, 053528.

Warren, B. E. (1969). *X-ray Diffraction.* Courier Corporation.

Wehrenberg, C. E., McGonegle, D., Bolme, C., Higginbotham, A., Lazicki, A., Lee, H. J., Nagler, B., Park, H.-S., Remington, B. A., Rudd, R. E., Sliwa, M., Suggit, M., Swift, D., Tavella, F., Zepeda-Ruiz, L. & Wark, J. S. (2017). *Nature*, **550**, 496–499.

Xiong, L., Bai, L. & Liu, J. (2014). *J. Appl. Phys.* **115**, 033509.

Yuan, G., Feng, R. & Gupta, Y. M. (2001). *J. Appl. Phys.* **89**, 5372–5380.

Zhao, S., Hahn, E. N., Kad, B., Remington, B. A., Wehrenberg, C. E., Bringa, E. M. & Meyers, M. A. (2016). *Acta Mater.* **103**, 519–533.